Epistatic, synthetic, and balancing interactions among tubulin missense mutations affecting neurite growth in *Caenorhabditis elegans*

Ho Ming Terence Lee[a], Natalie Yvonne Sayegh[b], A. Sophia Gayek[b], Susan Laura Javier Jao[b], Martin Chalfie[b,*], and Chaogu Zheng[a,*]
[a]School of Biological Sciences, The University of Hong Kong, Hong Kong SAR, China; [b]Department of Biological Sciences, Columbia University, New York, NY 10027

ABSTRACT **Mutations in tubulins affect microtubule (MT) dynamics and functions during neuronal differentiation and their genetic interaction provides insights into the regulation of MT functions. We previously used *Caenorhabditis elegans* touch receptor neurons to analyze the cellular impact of tubulin mutations and reported the phenotypes of 67 tubulin missense mutations, categorized into three classes: loss-of-function (*lf*), antimorphic (*anti*), and neomorphic (*neo*) alleles. In this study, we isolated 54 additional tubulin alleles through suppressor screens in sensitized backgrounds that caused excessive neurite growth. These alleles included 32 missense mutations not analyzed before, bringing the total number of mutations in our collection to 99. Phenotypic characterization of these newly isolated mutations identified three new types of alleles: partial *lf* and weak *neo* alleles of *mec-7*/β-tubulin that had subtle effects and strong *anti* alleles of *mec-12*/α-tubulin. We also discovered complex genetic interactions among the tubulin mutations, including the suppression of *neo* mutations by intragenic *lf* and *anti* alleles, additive and synthetic effects between *mec-7 neo* alleles, and unexpected epistasis, in which weaker *neo* alleles masked the effects of stronger *neo* alleles in inducing ectopic neurite growth. We also observed balancing between *neo* and *anti* alleles, whose respective MT-hyperstablizing and -destabilizing effects neutralized each other.**

Monitoring Editor
Jeff Hardin
University of Wisconsin, Madison

Received: Jul 29, 2020
Revised: Dec 9, 2020
Accepted: Dec 17, 2020

INTRODUCTION

Understanding how the regulation of microtubules (MTs) affects neurite growth at the single cell level is important for deciphering the molecular mechanisms of neuronal morphogenesis. The α/β-tubulin heterodimer is the building block of MTs, and mutations in the tubulin genes have profound effects on MT dynamics and cellular functions (Basciano *et al.*, 2015; Ti *et al.*, 2016). Clinical studies in the past decades have identified over 100 tubulin missense mutations associated with a wide range of neurodevelopmental disorders, including microcephaly, lissencephaly, pachygyria, polymicrogyria, and other cortical malformations, as well as the agenesis or hypoplasia of the corpus callosum, internal capsule, commissural fibers, and corticospinal tracts (Tischfield *et al.*, 2011). The diseases caused by mutations in tubulin genes are collectively termed "tubulinopathies" (Bahi-Buisson *et al.*, 2014). Besides their severe clinical symptoms, the cellular impact of those tubulin missense mutations on individual neurons is not well characterized. Moreover, the genetic interaction among the tubulin mutations in the context of neuronal differentiation, especially in axonal growth, is not well studied.

We previously established a platform to study the impact of tubulin mutations on neuronal growth using the touch receptor neurons (TRNs) of the nematode *Caenorhabditis elegans* (Zheng *et al.*, 2017). The TRNs have simple morphology and can be visualized by cell-specific expression of fluorescent proteins in live and free-moving animals. The two major TRN subtypes, ALM and PLM neurons,

---

*Address correspondence to: Martin Chalfie (mc21@columbia.edu); Chaogu Zheng (cgzheng@hku.hk).

Abbreviations used: *anti*, antimorph; *lf*, loss-of-function; MAP, MT-associated protein; MT, microtubule; *neo*, neomorph; PN, posterior neurite; TRN, touch receptor neuron; WT, wild type.

have well-defined cell shapes and neurite growth patterns (Figure 1, A and B). ALM neurons grow a single, anteriorly directed neurite, termed ALM-AN, and PLM neurons grow two neurites toward the anterior and the posterior, which are termed PLM-AN and PLM-PN, respectively. The simplicity of this neuronal structure offers the opportunity to quantitatively measure changes in neurite growth.

In our previous study, we analyzed the effects of 67 missense mutations in *mec-12*/α-tubulin and *mec-7*/β-tubulin, which are specifically expressed in the TRNs, on the neurite growth patterns of TRNs (Zheng *et al.*, 2017). Based on the phenotypes, we categorized those mutant alleles into three classes: loss-of-function (*lf*), antimorph (*anti*), and neomorph (*neo*). The *lf* mutations rendered the tubulin inactive and caused mild neurite growth defects likely due to the compensation from other tubulin isotypes; antimorphic gain-of-function mutations acted as dominant-negatives to block MT polymerization and caused severe neurite growth defects; and neomorphic gain-of-function mutations resulted in increased MT stability and excessive neurite growth, in particular the production of an ectopic ALM posterior neurite, termed ALM-PN (Zheng *et al.*, 2017). Structure–function analysis showed that *lf* mutations likely affected tubulin folding, *anti* mutations mostly affected residues in the GTP binding site and the intradimer and interdimer interfaces, and *neo* mutations, which were mapped to the exterior surface of the α/β-tubulin dimmer, were hypothesized to affect the interaction with MT-associated proteins (MAPs). Because of the hyperstable MTs and the generation of an ectopic ALM-PN in the *neo* strains, they provide a sensitized background that can be used to identify genes that contribute to MT stability and neurite growth, especially for genes whose mutations may not lead to significant changes in neuronal morphology in the otherwise wild-type (WT) background. Such suppressor screens may also identify mutations whose products interact genetically with the tubulin neomorphs.

mec-12 and *mec-7* are not the only genes that can be mutated to cause excessive neurite growth of the TRNs. For example, *lf* mutations in a MT-depolymerizing kinesin-13 gene *klp-7* resulted in the generation of an ectopic ALM-PN, presumably due to elevated MT stability (Zheng *et al.*, 2017). Moreover, the loss of α-tubulin acetyltransferase gene *mec-17* also induced the production of an ALM-PN, although this regulation of neurite growth was independent of the enzymatic activity of MEC-17 (Topalidou *et al.*, 2012). Those mutants can also be used in suppressor screens to identify genes regulating MT dynamics and neurite growth.

In this study, we describe two forward genetic screens that identified suppressors of ectopic ALM-PN growth in *mec-7(neo)* and *mec-17(lf)* mutants, respectively. The two screens yielded 54 alleles in *mec-7* and *mec-12*, of which 46 are missense alleles. These mutations included 32 new missense mutations. The addition of these new alleles brings the total number of tubulin missense mutations in our collection to 99. The phenotypic classification and structure–function analysis of these mutations provide a resource for understanding the functional impact of tubulin mutations on neuronal morphogenesis at the cellular level. The analysis of the newly isolated alleles defined three new types of tubulin alleles: partial *lf* alleles in *mec-7* that specifically disrupted the growth of the PLM synaptic branch, weak *mec-7(neo)* alleles that caused the overextension of PLM-PN but did not induce the growth of an ectopic ALM-PN, and strong *mec-12(anti)* alleles that shortened all TRN neurites. Moreover, we found unexpected genetic interactions among the tubulin alleles, including the epistatic and synthetic interactions among the *mec-7(neo)* alleles, as well as a counterbalance between the effects of *neo* and *anti* mutations.

RESULTS

Genetic screens for suppressors of the ALM-PN phenotype yielded many *mec-7* and *mec-12* alleles

Among the tubulin *neo* mutations, *mec-7(u278)* produced the strongest phenotype with a very long ALM-PN that often extended to the tail region (Figure 1C). Leveraging this clear phenotype, we conducted a suppressor screen to search for mutations that can suppress the growth of the ectopic ALM-PN in *mec-7(u278neo)* mutants. We screened 53,600 haploid genomes and isolated 30 suppressors. Genetic mapping and whole-genome resequencing identified the phenotype-causing mutations in these suppressors, including 19 intragenic mutations in *mec-7* (two nonsense alleles, one deletion allele, and 16 missense alleles), nine mutations in *mec-12* (one deletion allele and 8 missense alleles), one mutation in *mec-15*, and one mutation in *mbl-1* (Supplemental Table S1). *mec-15* codes for an F-box domain and WD40 repeats-containing protein, whose role in regulating MT organization and neurite growth was previously reported (Zheng *et al.*, 2020). *mbl-1* codes for an RNA splicing regulator, whose function in the TRNs will be discussed elsewhere. In this study, we focus on the effects of *mec-7* and *mec-12* missense mutations on neuronal morphogenesis.

Deletion of *mec-17*, which encodes an α-tubulin acetyltransferase (Akella *et al.*, 2010), alters MT structure and induces the growth of an ectopic ALM-PN (Topalidou *et al.*, 2012). Compared with *mec-7(u278neo)* animals, the ALM-PN in *mec-17(lf)* mutants was much shorter and only occurred in L4 and adult animals (Figure 1E and Supplemental Supplemental Figure S1A). We reason that the late onset of the ALM-PN phenotype in *mec-17(lf)* mutants may allow us to isolate suppressors different from the suppressors of *mec-7(u278neo)*. In the *mec-17(lf)* suppressor screen, we isolated 16 mutations in *mec-7* (two nonsense alleles, one splice variant, and 13 missense alleles), 10 mutations in *mec-12* (one start-loss allele and nine missense alleles; Supplemental Table S2), and five nontubulin mutations that will be described elsewhere. Thus, from the two suppressor screens, we identified 29 *mec-7* missense alleles and 17 *mec-12* missense alleles in total. The identification of *mec-7* and *mec-12* mutations as suppressors of the ALM-PN phenotype suggested that the generation of ectopic neurites in TRNs may require the incorporation of the MEC-12/MEC-7 (α/β tubulin) heterodimers into the MTs.

An updated catalogue of tubulin missense mutations affecting neurite growth

We previously reported the effects of 48 *mec-7* and 19 *mec-12* missense mutations on the growth of TRN neurites and categorized them into three classes (*lf*, *anti*, and *neo*), each with distinct morphological phenotypes (Zheng *et al.*, 2017). The screens described in this study added 20 new *mec-7* and 12 new *mec-12* missense mutations to this collection (Table 1). Since these mutations suppressed the growth of ectopic neurites, we expected them to generally reduce MT stability, although there were a few exceptions (see below).

To study the effect of each mutation on TRN morphogenesis, we removed *mec-7(u278neo)* from the *mec-12* alleles obtained in the *mec-7(neo)* suppressor screen and removed *mec-17(lf)* mutations from the *mec-7* and *mec-12* alleles isolated in the *mec-17(lf)* suppressor screen through outcrossing. We then examined how the tubulin mutations affected TRN neurite growth in the otherwise WT background. For the intragenic *mec-7* mutants isolated from the *mec-7(neo)* suppressor screen, it was technically impossible to remove the *mec-7(u278neo)* background through outcross, but we assumed the *mec-7* suppressor alleles could mask the effects of *mec-7(u278neo)*, allowing us to examine the single mutants' phenotype. For example, G141E mutation was previously identified as a

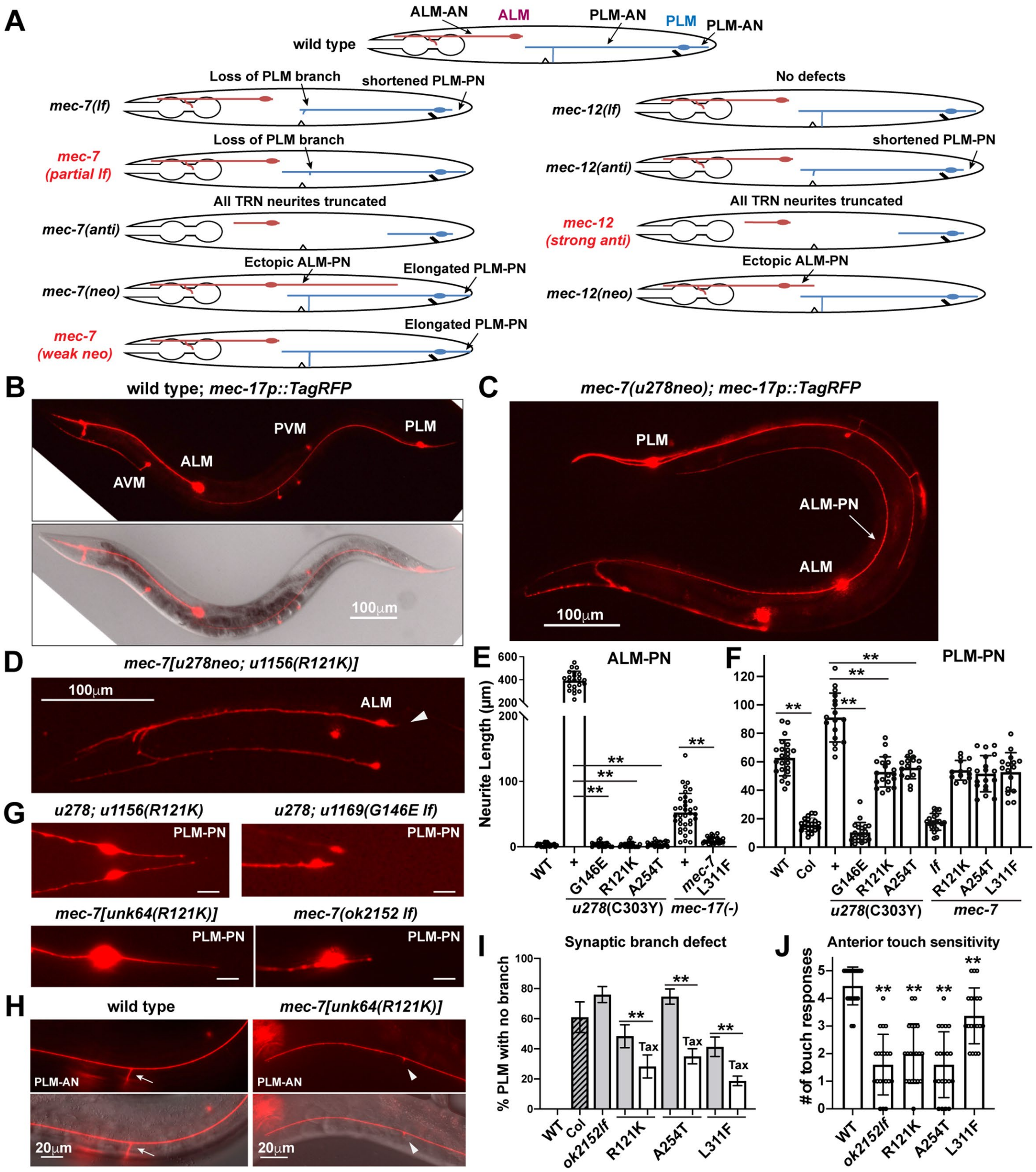

FIGURE 1: Partial *lf* mutations in *mec-7* suppressed ectopic neurite growth and led to the loss of the synaptic branch. (A) Schematic diagram of ALM and PLM morphologies in *mec-7* and *mec-12 lf, anti,* and *neo* mutants, as well as the three newly identified types of alleles—partial *lf* and weak *neo* alleles of *mec-7* and strong *anti* alleles of *mec-12*. (B–D) TRN morphology was visualized by TagRFP expressed from the TRN-specific *mec-17* promoter. Compared with the WT animals, *mec-7(u278neo)* animals had a very long, ectopic ALM-PN (arrow), whose generation was suppressed by intragenic partial *lf* mutation R121K. Arrowhead indicates the absence of ALM-PN. (E, F) Length of ALM-PN and PLM-PN in young adults of various strains. "Col" means colchicine treatment of the WT animals. Double asterisks indicate statistically significant differences ($p < 0.01$) in a Dunnett's test. (G) PLM-PN was significantly shortened in *u278*(C303Y *neo*) *u1169*(G146E *lf*) double mutants and *mec-7(ok2152)* deletion mutants but not in *u278 u1156*(R121K partial *lf*) and *unk64*(R121K) mutants. (H) Some *unk64* mutants did not extend a synaptic branch from PLM-AN. (I) The percentage of PLM neurons that lost the synaptic branch in various *mec-7* mutants. "Col" means colchicine treatment and "Tax" means taxol treatment. (J) The number of responses to five anterior gentle touches in young adults of indicated *mec-7* mutants.

mec-7 lf allele (Table 1), and *u278*(C303Y) *u1157*(G141E) double mutants showed the same *lf* phenotype (shortening of PLM-PN) as the G141E single mutants. This strategy was effective in identifying the effects of most *mec-7* intragenic suppressors except for four alleles, whose phenotype appeared to be ambiguous and did not fall into any phenotypical classification we previously established. To study the phenotypes of those four *mec-7* missense mutations by themselves, we recreated them in the WT animals using CRISPR-mediated genome editing and examined their effects on TRN morphology (asterisks in Table 1).

Gene	Alleles	Mutation	Structural function	Classification	Morphological defects	Touch sensitivity
mec-7	*u1123*	E3K	Lumen-facing loop	Loss-of-function	Shortened PLM-PN	–
	u1151	C12Y	GTP binding	Loss-of-function	Shortened PLM-PN	–
	u1152	G13S	GTP binding	Loss-of-function	Shortened PLM-PN	–
	u319, *u1153*, *u1118*, *u1120*	S25F	Tubulin folding	Weak antimorph	Moderately shortened neurites	–
	u305, *u1020*, *u1124*	G34S	Lumen-facing loop	Loss-of-function	Shortened PLM-PN	±
	gk906464	G38E	Lumen-facing loop	N/A	No defects	+
	u58, *u223*	P61L	Lumen-facing loop	Weak antimorph	Moderately shortened neurites	–
	u249	P61S	Lumen-facing loop	Weak antimorph	Moderately shortened neurites	–
	gk337318	V64I	Tubulin folding	N/A	No defects	+
	u1154	E69K	GTP binding	Antimorph	Shortened TRN neurites	–
	u1155	G71E	Tubulin folding	Loss-of-function	Shortened PLM-PN	–
	u1115	R86C	Lumen-facing loop	Weak neomorph	Overextended PLM-PN	±
	u430	A97V	GTP binding	Antimorph	Shortened TRN neurites	–
	u1040	G98E	GTP binding	Loss-of-function	Shortened PLM-PN	–
	u222	G109E	Lateral interaction	Weak antimorph	Moderately shortened neurites	–
	u1156, *unk64**	R121K	Lateral interaction	Partial loss-of-function	No PLM synaptic branch	±
	u429, *u433*, *u1157*	G141E	GTP binding	Loss-of-function	Shortened PLM-PN	–
	gk595364	G141R	GTP binding	Loss-of-function	Shortened PLM-PN	–
	u1122	S145F	Tubulin folding	Loss-of-function	Shortened PLM-PN	–
	u1169	G146E	Tubulin folding	Loss-of-function	Shortened PLM-PN	–
	u275	G148R	Tubulin folding	Loss-of-function	Shortened PLM-PN	–
	gk895768, *u1158*	T149I	Tubulin folding	Neomorph	Ectopic ALM-PN	±
	gk286003	R162Q	MAP binding	Neomorph	Ectopic ALM-PN	±
	u911	P171S	GTP binding	Antimorph	Shortened TRN neurites	–
	u957, *u127*, *e1343*, *u1119*	P171L	GTP binding	Antimorph	Shortened TRN neurites	–
	u1056	S172P	GTP binding	Loss-of-function	Shortened PLM-PN	–
	u1057	P173L	GTP binding	N/A	No defects	+
	u48	S176F	GTP binding	Antimorph	Shortened TRN neurites	–
	u449	V179A	GTP binding	Antimorph	Shortened TRN neurites	–
	u10	S188F	Tubulin folding	Loss-of-function	Shortened PLM-PN	±
	u1160	D203V	GTP binding	Loss-of-function	Shortened PLM-PN	–
	u225	T214P	Tubulin folding	Loss-of-function	Shortened PLM-PN	±
	ky852	P220S	Tubulin folding	Neomorph	Ectopic ALM-PN	–
	u1114	G223E	Lateral interaction	Weak neomorph	Overextended PLM-PN	–
	u1110	L225F	Lateral interaction	Antimorph	Shortened TRN neurites	–

TABLE 1: The *mec-7* and *mec-12* mutations analyzed for the effects on TRN neurite growth. (*Continues*)

Gene	Alleles	Mutation	Structural function	Classification	Morphological defects	Touch sensitivity
	u262	N226Y	GTP binding	Antimorph	Shortened TRN neurites	–
	gk286002	P243S	Intradimer interaction	Loss-of-function	Shortened PLM-PN	±
	u283	P243L	Intradimer interaction	Antimorph	Shortened TRN neurites	–
	u129, *u958*	G244S	Intradimer interaction	Antimorph	Shortened TRN neurites	–
	n434	N247I	Intradimer interaction	Antimorph	Shortened TRN neurites	–
	u162, *u1117*	D249N	Intradimer interaction	Antimorph	Shortened TRN neurites	–
	unk22, *unk62**	A254T	Intradimer interaction	Partial loss-of-function	No PLM synaptic branch	–
	e1505	G269D	Tubulin folding	Loss-of-function	Shortened PLM-PN	±
	e1527	V286D	Lateral interaction	Antimorph	Shortened TRN neurites	–
	u445	M300V	Tubulin folding	Antimorph	Shortened TRN neurites	–
	u98	M300T	Tubulin folding	Antimorph	Shortened TRN neurites	–
	u1058	A302T	MAP binding	Neomorph	Ectopic ALM-PN	±
	u1161, *unk60**	A302V	MAP binding	Neomorph	Ectopic ALM-PN	±
	u278	C303Y	MAP binding	Neomorph	Ectopic ALM-PN	–
	gk286001	C303S	MAP binding	N/A	No defects	+
	u1147	L311F	Tubulin folding	Partial loss-of-function	No PLM synaptic branch	±
	gk286000	A314V	Tubulin folding	Antimorph	Shortened TRN neurites	–
	e1522	F317I	Tubulin folding	Loss-of-function	Shortened PLM-PN	±
	u234	R318Q	Tubulin folding	Loss-of-function	Shortened PLM-PN	±
	u955	A352T	Intradimer interaction	Antimorph	Shortened TRN neurites	–
	u1116	P357S; Q424L	Lumen-facing loop	Loss-of-function	Shortened PLM-PN	–
	u910, *gk373602*	P357L	Lumen-facing loop	Antimorph	Shortened TRN neurites	–
	u956	P358L	Lumen-facing loop	Antimorph	Shortened TRN neurites	–
	u1170	P358S	Lumen-facing loop	Antimorph	Shortened TRN neurites	–
	u428, *u1113*	G369E	Tubulin folding	Loss-of-function	Shortened PLM-PN	–
	u1017	L377F	MAP binding	Neomorph	Ectopic ALM-PN	±
	u1059	R380S	MAP binding	Neomorph	Ectopic ALM-PN	±
	u1171, *unk63**	R391H	MAP binding	Antimorph	Shortened TRN neurites	–
	u18	A393T	Longitudinal interaction	Antimorph	Shortened TRN neurites	–
	gk285997	A393V	Longitudinal interaction	Antimorph	Shortened TRN neurites	–
	u1164	G402R	Longitudinal interaction	Loss-of-function	Shortened PLM-PN	–
	u170	E407L	MAP binding	Neomorph	Ectopic ALM-PN	±
	u1060	E410K	MAP binding	Antimorph	Shortened TRN neurites	–
mec-12	*u1172*	G13E	Tubulin folding	Antimorph	Shortened PLM-PN	–

TABLE 1: The *mec-7* and *mec-12* mutations analyzed for the effects on TRN neurite growth.

(*Continues*)

Gene	Alleles	Mutation	Structural function	Classification	Morphological defects	Touch sensitivity
	u1129	A19V	Tubulin folding	Antimorph	Shortened PLM-PN	–
	gk170196	P32S	Lumen-facing loop	Neomorph	Ectopic ALM-PN	±
	gk170195	S50N	Lumen-facing loop	N/A	No defects	+
	gk636747	R60H	Lumen-facing loop	N/A	No defects	+
	u1131	P63S	Lumen-facing loop	Neomorph	Ectopic ALM-PN	±
	u76	D69N	GTP binding	Antimorph	Shortened PLM-PN	–
	u1132	E71K	Intradimer interaction	Antimorph	Shortened PLM-PN	–
	u1016	E97K	Intradimer interaction	Antimorph	Shortened PLM-PN	–
	u1174	G134E	Tubulin folding	Strong antimorph	Shortened PLM-PN	–
	u950, *gk672907*	S140F	GTP binding	Antimorph	Shortened PLM-PN	–
	gk600523	G142E	GTP binding	Loss-of-function	No defects	±
	u1021, *e1607*	G144S	GTP binding	Antimorph	Shortened PLM-PN	–
	gk583647	L152F	Tubulin folding	N/A	No defects	+
	u1128	S178F	GTP binding	Strong antimorph	Shortened PLM-PN	–
	u50, *e1605*	H192Y	MAP binding	Partial loss-of-function	No defects	–
	gk915672	E196K	MAP binding	Neomorph	Ectopic ALM-PN	±
	u1126	S236N	Tubulin folding	Antimorph	Shortened PLM-PN	–
	u1134	A240T	Tubulin folding	N/A	No defects	+
	u1127	S241F	Tubulin folding	Antimorph	Shortened PLM-PN	–
	u1041, *unk46*, *u1135*	G246E	Longitudinal interaction	Antimorph	Shortened PLM-PN	±
	u1175	T257K	Longitudinal interaction	Antimorph	Shortened PLM-PN	–
	u917	V260I	MAP binding	Neomorph	Ectopic ALM-PN	±
	gk854211	P307L	MAP binding	N/A	No defects	+
	u1133	R320C	Tubulin folding	Antimorph	Shortened PLM-PN	–
	gk515972	V323I	Tubulin folding	Neomorph	Ectopic ALM-PN	±
	unk23	G350E	Longitudinal interaction	Antimorph	Shortened PLM-PN	–
	u241, *u1019*, *u1165*	G354E	Longitudinal interaction	Antimorph	Shortened PLM-PN	–
	gk341552	G365E	Lumen-facing loop	N/A	No defects	+
	u63, *u1176*	E415K	MAP binding	Partial loss-of-function	No defects	±
	gm379, *u1177*	G416E	MAP binding	Partial loss-of-function	No defects	±

Alleles in black were previously analyzed (Zheng *et al*., 2017); alleles in red were isolated from the *mec-7(u278 neo)* suppressor screen; alleles in blue were isolated from the *mec-17(-)* suppressor screen. For touch sensitivity, (+) indicates the average response to five anterior stimuli is above 4; (±) indicates the average is between 4 and 1; (–) indicates the average is below 1. Asterisks indicate the alleles created through CRISPR/Cas9-mediated genome editing. Amino acid residues affected by the missense mutations were mapped to the *B. taurus* α/β-tubulin structures (Nogales *et al*., 1998).

TABLE 1: The *mec-7* and *mec-12* mutations analyzed for the effects on TRN neurite growth. Continued

A few *mec-7* and *mec-12* missense mutations were repeatedly isolated. For example, antimorphic S25F mutation in MEC-7 and G246E mutation in MEC-12 was isolated in previous screens using WT background and in both suppressor screens of this study. Overall, 11 missense mutations were recovered in more than one screen. Importantly, alleles that carry the same mutation but were independently isolated showed the same phenotype, suggesting that our system of phenotyping generated consistent results.

In summary, among the 20 newly found *mec-7*/β-tubulin missense alleles, 10 were *lf* alleles with clearly shortened PLM-PN and three were partial *lf* alleles that caused the loss of PLM synaptic branch but had normal length of PLM-PN (those partial *lf* alleles were not identified before and thus defined a new phenotypic category). Four were *anti* alleles that caused the shortening of all TRN neurites. The remaining three mutations were *neo* alleles that caused either the growth of ectopic ALM-PN or overextension of PLM-PN (two weak *neo* alleles had very low penetrance of ectopic ALM-PN phenotype and mostly caused the production of longer PLM-PNs, thus defining a new phenotypic category). The 12 newly isolated *mec-12*/α-tubulin missense alleles included 10 *anti* alleles that led to the shortening of PLM-PN, one *neo* allele that induced the growth of an ectopic ALM-PN, and one allele that appeared not to cause any phenotype by itself (Table 1). Moreover, *lf* alleles were mostly recessive, whereas *anti* and *neo* alleles were often dominant or semidominant.

Combining this study with our previous work (Zheng *et al.*, 2017), we report the neuronal phenotype of a total of 99 tubulin missense mutations (68 β-tubulin and 31 α-tubulin mutations) represented by 127 alleles isolated or engineered independently (Table 1). Given the very high evolutionary conservation of tubulin amino acid sequences across species (identity > 95%), this large collection of tubulin mutants and their phenotypic characterization can serve as a resource for understanding the relationship of tubulin dimer structure with MT stability and neurite development in general.

Suppression of ectopic ALM-PN growth by tubulin *lf* and *anti* alleles

Among the 16 *mec-7* intragenic missense mutations that suppressed the long ectopic ALM-PN caused by *mec-7(u278)* allele, 10 are *lf* alleles, four are antimorphs, and two are neomorphs. The eight *mec-12* missense alleles that suppressed *mec-7(u278)* included four *lf* alleles and four *anti* alleles. Among the missense mutations that suppressed ALM-PN growth caused by the *mec-17* deletion, there were six *lf* alleles, five *anti* alleles, and two *neo* alleles of *mec-7*; and one *lf* allele, six *anti* alleles, and one *neo* allele of *mec-12* (Table 1). Thus, 89% of the suppressors are either tubulin *lf* or *anti* alleles, which down-regulate MT stability and limit neurite growth.

Interestingly, three *mec-7* mutations, R121K, A254T, and L311F, defined a new type of *lf* alleles (R121K and A254T were recreated in the otherwise WT animals through CRISPR gene editing). The three mutations suppressed the ALM-PN production (Figure 1, D and E) but did not show a clear *lf* phenotype by themselves. For example, they did not cause the shortening of PLM-PN as seen in the *mec-7* deletion alleles (Figure 1, F and G). They did, however, cause the loss of synaptic branch in PLM-AN and the reduction of touch sensitivity (Figure 1, H and J), which were also seen with the *mec-7* deletion alleles. Because only part of the *lf* phenotypes was observed in these mutants, we classified them as partial *lf* alleles. The loss of the synaptic branch also led to disrupted transport of GFP-fused synaptic vesicle protein RAB-3. For PLM-ANs that had no clear branching point, we did not observe GFP::RAB-3 signal along the neurite; for PLM-ANs that had a very short branch, weak GFP::RAB-3 signal was observed at the branching site (Supplemental Figure S2, A and B).

We also found a new type of *mec-12 anti* alleles in this study. Previously, we classified *mec-12 anti* alleles as mutants that mostly shortened PLM-PN but not ALM-AN and PLM-AN and thought that *mec-12 anti* mutations had a weaker effect than *mec-7 anti* mutations, which caused the shortening of all TRN neurites (Figure 1A). Eight of the 10 new *mec-12 anti* alleles isolated in the suppressor screens indeed fit this phenotypic classification, but the other two alleles, *u1174*(G134E) and *u1128*(S178F), produced much stronger phenotypes, showing severe defects in the extension of ALM-AN, PLM-AN, and PLM-PN, similar to the phenotype of *mec-7 anti* alleles (Figure 2, A–C). Both mutations also caused excessive sprouting from PLM-AN, possibly the result of increased MT dynamics (Figure 2B). MT depolymerization induced a general down-regulation of protein expression in TRNs (Bounoutas *et al.*, 2011). As a result, the level of TagRFP proteins (measured by fluorescent intensity) expressed from a TRN-specific promoter was down-regulated in tubulin mutants compared with the WT. We found that the TagRFP level was much lower in *u1174* and *u1128* mutants than in other *mec-12 anti* mutants, consistent with further reduced MT stability (Figure 2D). Since the phenotypes caused by these changes were more severe than the *mec-12 anti* alleles characterized before, we classified them as strong antimorphs (Table 1). These results suggest that, unlike previously thought, dominant-negative MEC-12 mutants can be as disruptive as the MEC-7 *anti* mutants in affecting TRN neurite growth.

Pharmacological studies supported that the TRN morphological defects in tubulin *lf* and *anti* mutants resulted from decreased MT stability. First, treatment with the MT-destabilizing agent colchicine in the WT animals shortened PLM-PN and caused the loss of PLM synaptic branch, similar to *mec-7(lf)* phenotypes (Figure 1, F and I). Second, MT-stabilizing drug paclitaxel (taxol) rescued the branching defects in *mec-7* partial *lf* mutants (Figure 1I and Supplemental Figure S3). Third, taxol treatment also partially suppressed the severe neurite growth defects in *mec-7* and *mec-12 anti* alleles (Figure 2C and Supplemental Figure S3).

Moreover, we also analyzed MT dynamics by tracking the MT-plus end binding protein EBP-2. MTs in WT animals are very stable and we could only observe a few EBP-2::GFP tracks in PLM neurites. However, *mec-7(lf)* mutants showed an increased number of EBP-2 tracks in PLM-AN and PLM-PN, and *mec-7(anti)* mutants had even more tracks (Figure 3, A and B). Furthermore, we found that MTs in PLM-AN maintained a largely uniform "plus-end-out" polarity and MTs in PLM-PN showed mixed polarity in WT animals, which is consistent with a previous observation (Hsu *et al.*, 2014). Interestingly, MTs in both PLM-AN and PLM-PN had mixed polarity in *mec-7 lf* and *anti* mutants (Figure 3A and B). Increased MT dynamics and altered MT polarity in these mutants may have caused the defects in neurite extension.

Structure–function relationships of tubulin mutations

Our previous studies revealed that the different types of tubulin missense mutations affected distinct parts of the molecules (Zheng *et al.*, 2017). For example, the amino acids altered by *lf* mutations tend to be distributed throughout the molecules and often likely affected tubulin folding, whereas *anti* mutations altered residues involved in GTP/GDP binding and intradimer or interdimer interactions. This pattern is also supported by newly isolated *mec-7* and *mec-12* alleles. In total, 13 amino acids in the GDP binding pocket of MEC-7/β-tubulin (the E site) and five amino acids in the GTP binding pocket of MEC-12/α-tubulin (the N site) were affected by the *lf*

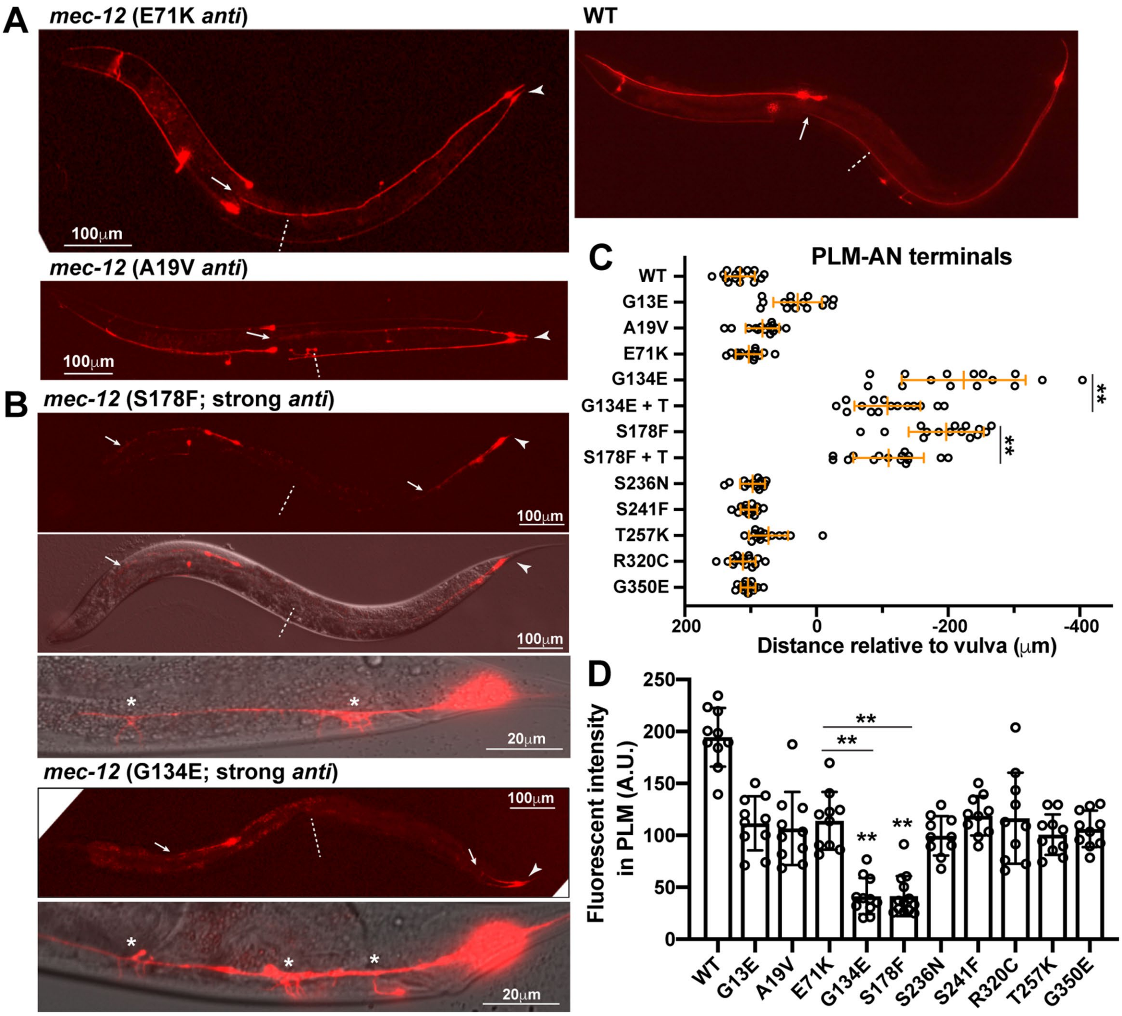

FIGURE 2: Strong *anti* alleles of *mec-12* led to severe shortening of TRN neurites. (A) *mec-12 anti* mutations mostly shortened PLM-PN (arrowhead) but not PLM-AN. Arrow points to the terminal of PLM-AN and dashed line indicates the position of the vulva. (B) Strong *anti* mutations of *mec-12* resulted in the shortening of not only PLN-AN (arrowed head) but also PLM-AN and ALM-AN (arrows). PLM-AN failed to reach the vulva (dashed line) and had excessive sprouting (asterisks). (C) Distance from the PLM-AN terminals to the vulva in various *mec-12* mutants. Positive numbers mean that PLM-AN grew pass the vulva and negative numbers mean that PLM-AN did not reach the vulva. The "+ T" means taxol treatment of specific mutants. Double asterisks indicate a significant difference ($p < 0.01$) compared with the WT in a Dunnett's test. (D) Fluorescent intensity of PLM neurons expressing the same *mec-17p::TagRFP* transgene measured under the same condition in various mutants. Intensity is in arbitrary units (A.U.).

or *anti* alleles (Figure 4, A and B; red for *lf* mutations and blue for *anti* mutations); C12Y, G13S, G98E, and D203V mutations in MEC-7 and S178F in MEC-12 were identified in this study.

Using the structure editing function of ChimeraX, which is based on a smoothed backbone-dependent rotamer library (see *Materials and Methods*; Shapovalov and Dunbrack, 2011), we found that the amino acid substitutions in those missense alleles often caused steric clashes with the GDP molecule and/or other residues in the binding pocket. For instance, C12Y mutation led to direct clashes with the guanine on the GDP molecule and I16 and V169 surrounding the pocket; G13S led to clashes with H137 and A9 residues (Figure 4C). Similarly, previously identified *lf* mutations G141E and G141R led to severe clashes with the phosphate groups from the GDP molecules (Figure 4D). Thus, those amino acid substitutions likely rendered the MEC-7 mutants incapable of binding to GTP/GDP, thus creating a *lf* phenotype. The substitutions in the *anti* alleles (Figure 4) may cause MEC-7 to bind GTP/GDP in an abnormal way that blocks further polymerization, thus creating dominant-negative phenotypes.

Our study also identified seven more residues involved in tubulin intradimer or interdimer interactions that are altered in *lf* and *anti* alleles, bringing the total number of such residues to 20 (Figure 4, E–H). For example, at the intradimer interface, previous work found that P243L, G244S, N247I, and D249N mutations affecting the H7-to-H8 (the seventh helix to the eight helix) loop of MEC-7 all caused the *anti* phenotype with severely shortened TRN neurites (Zheng *et al.*, 2017). In this study, we found that mutation of E71 in MEC-12, which makes direct contact with N247 in MEC-7, also creates *anti* phenotypes. The E71K substitution is predicted to cause clashes with N247 on β-tubulin (Figure 4F), which might lead to the formation of misshapen tubulin dimers and the termination of polymerization. We also found *anti* mutations affecting longitudinal interdimer interactions (T257K and G350E in MEC-12) and lateral interactions (L225F in MEC-7). These defects support the hypothesis that

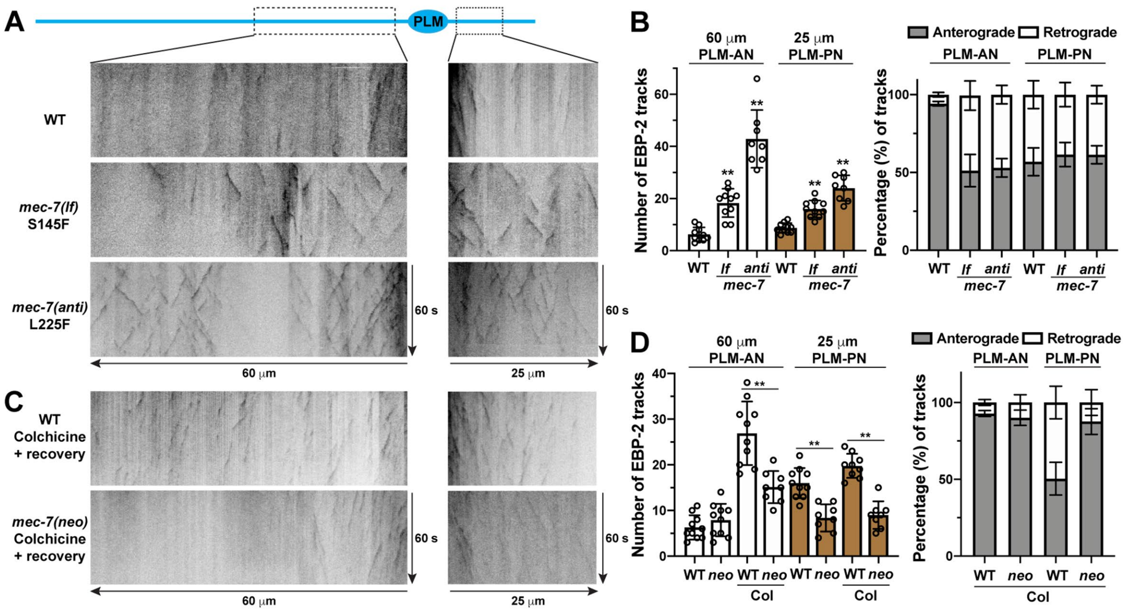

FIGURE 3: MT dynamics and polarity in *mec-7 lf*, *anti*, and *neo* mutants. (A) Representative kymographs of MT dynamics in the PLM-AN and PLM-PN of adult WT, *mec-7(u1122lf;* S145F), and *mec-7(u1110anti;* L225F*)* animals. (B) The total number of EBP-2::GFP comets in a 60-μm segment of PLM-AN and a 25-μm segment of PLM-PN from the cell body in WT, *mec-7(u1122lf)*, and *mec-7(u1110anti)* animals. The fraction of MTs with plus-end-out (anterograde direction comets) and "minus-end-out" (retrograde direction comets) polarity in PLM-AN and PLM-PN. (C) Representative kymographs of MT dynamics in WT and *mec-7(u278neo;* C303Y*)* animals, which were treated with 0.125 mM colchicine for 8 h at L4 stage and then recovered on regular NGM plates for 1 h. (D) The number of EBP-2::GFP comets and the fraction of the comets in anterograde and retrograde directions in the treated WT and *mec-7(u278neo)* animals.

disrupting tubulin dimer stacking can generate dominant-negative effects. Two *mec-7* partial *lf* alleles affected intradimer interaction (A254T) and lateral interdimer interaction (R121K), and one *lf* allele altered a residue involved in longitudinal interaction (G402R); these mutant dimers may be structurally compromised and might reduce MT stability when incorporated. The third *mec-7* partial *lf* allele had L311F substitution, which was mapped to the interior of the tubulin structure and may affect tubulin folding.

Epistasis among the *mec-7 neo* mutations

The isolation of *neo* mutations from the *mec-7(u278)* suppressor screen looking for suppressors of ALM-PN was rather surprising. Two *mec-7* intragenic mutations, T149I and A302V, were found to strongly suppress the growth of the long ALM-PN induced by *mec-7(u278)* allele (Figure 5, A and B). T149I substitution was previously characterized as a *neo* mutation because the *gk895768* allele carrying the same mutation caused the growth of an ectopic ALM-PN; A302V was recreated in the WT background using CRISPR gene editing and was found to induce the production of an ALM-PN by itself. In both cases, the length of ALM-PN induced by T149I and A302V mutations alone was much shorter than the long ALM-PN induced by *u278*(C303Y) and similar to the mutants carrying double missense mutations (Figure 5, A and B). Thus, T149I and A302V mutations appeared to be intramolecularly epistatic to C303Y mutations in their effects on inducing excessive neurite growth.

Pharmacological studies suggest that the *neo* mutations induce the growth of excessive ALM-PN likely by elevating MT stability. The MT-stabilizing agent taxol induced the growth of a short ALM-PN, and treatment with the MT-destabilizing drug colchicine eliminated the ALM-PN in *mec-7(neo)* mutants (Figure 5B). Moreover, *mec-7(neo)* mutants have reduced MT dynamics and higher resistance to colchicine compared with the WT animals. Using a mild colchicine treatment (0.125 mM for 8 h) followed by a 1-h recovery, we were able to significantly increase MT dynamics and observed more EBP-2::GFP tracks in the WT animals. *mec-7(neo)* mutants showed much fewer tracks than the WT animals under the same condition (Figure 3, C and D). Interestingly, *mec-7(neo)* mutants showed a more uniform (plus-end-out) MT polarity in PLM-PN compared with the mixed polarity in the WT animals. Reduced dynamics and uniform polarity may lead to the elongation of PLM-PN in *mec-7(neo)* animals. We were not able to observe consistent EBP-2 comets in ALM neurites in WT and *mec-7(neo)* mutants with or without the colchicine treatment.

With regard to structure–function relationships, *neo* mutations might increase MT stability by affecting the binding of MAPs. For example, *neo* mutations L377F, R380S, and E407L affected residues on helices H11 and H12, which are the major landing surface for MAPs (Nogales *et al.*, 1998); R162Q was mapped to the H4-to-B5 loop, which is exposed to the exterior of MTs. As the strongest *neo* allele with the longest ALM-PN, *u278*(C303Y) altered C303 in the H9-to-B8 loop, which is adjacent to H11 and is also exposed on the exterior surface of MTs (Figure 6A). Structural modeling suggested that C303Y substitution would lead to steric clashes between the benzene ring of the tyrosine and E376 and L377 on the H11 with 60% probability or clashes with M267 on B7 (the seventh β-strand) with 18% probability, depending on the orientation of the phenyl group (Figure 6C). In contrast, C303S substitution did not generate any clashes in our analysis (Figure 6D), which is consistent with the findings that the *gk286001*(C303S) allele did not cause any TRN morphological defects. Thus, we hypothesize that the bulkiness of tyrosine might have pushed H11 out of its normal position, which altered the binding of certain MAPs and resulted in abnormally elevated MT stability.

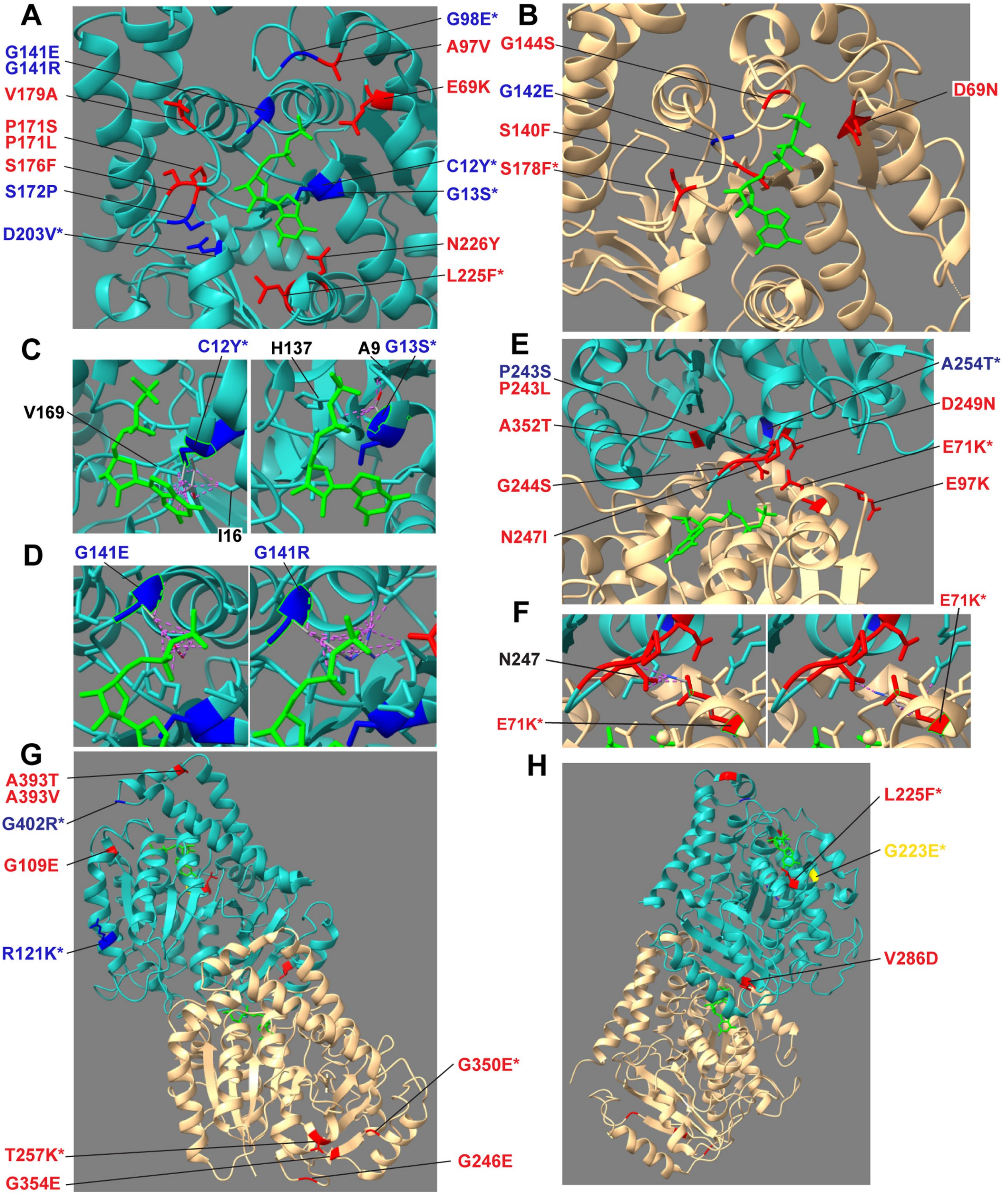

FIGURE 4: Positions of amino acid residues changed in *mec-7* and *mec-12 lf* and *anti* mutants. The structure of the α/β-tubulin dimer (1jff.pdb) was visualized using ChimeraX with β-tubulin in cyan, α-tubulin in wheat, and GTP/GDP in green. (A, B) Amino acid substitutions around the GTP (green) binding pocket in *mec-7* and *mec-12 lf* (blue) and *anti* (red) alleles. For the entire figure, substitutions without an asterisk were previously analyzed and substitutions with an asterisk are from this study. (C) C12Y mutation leads to clashes with V169 residue and G13S mutation leads to clashes with A9 and H137 residues. (D) G141E and G141R mutations lead to clashes with the GTP molecules. (E) *mec-7* and *mec-12 lf* (blue) and *anti* (red) mutations mapped to the intradimer interface. (F) E71K substitution in MEC-12 leads to clashes with N247 on MEC-7. Two possible orientations of the substituting lysine are shown. In C, D, and F, gray sticks show the substituting residues and purple dashed lines indicate steric clashes. (G, H) *mec-7* and *mec-12 lf* (blue) and *anti* (red) mutations mapped to interdimer interface. G223E substitution (yellow) was found in a weak *neo* allele of *mec-7*.

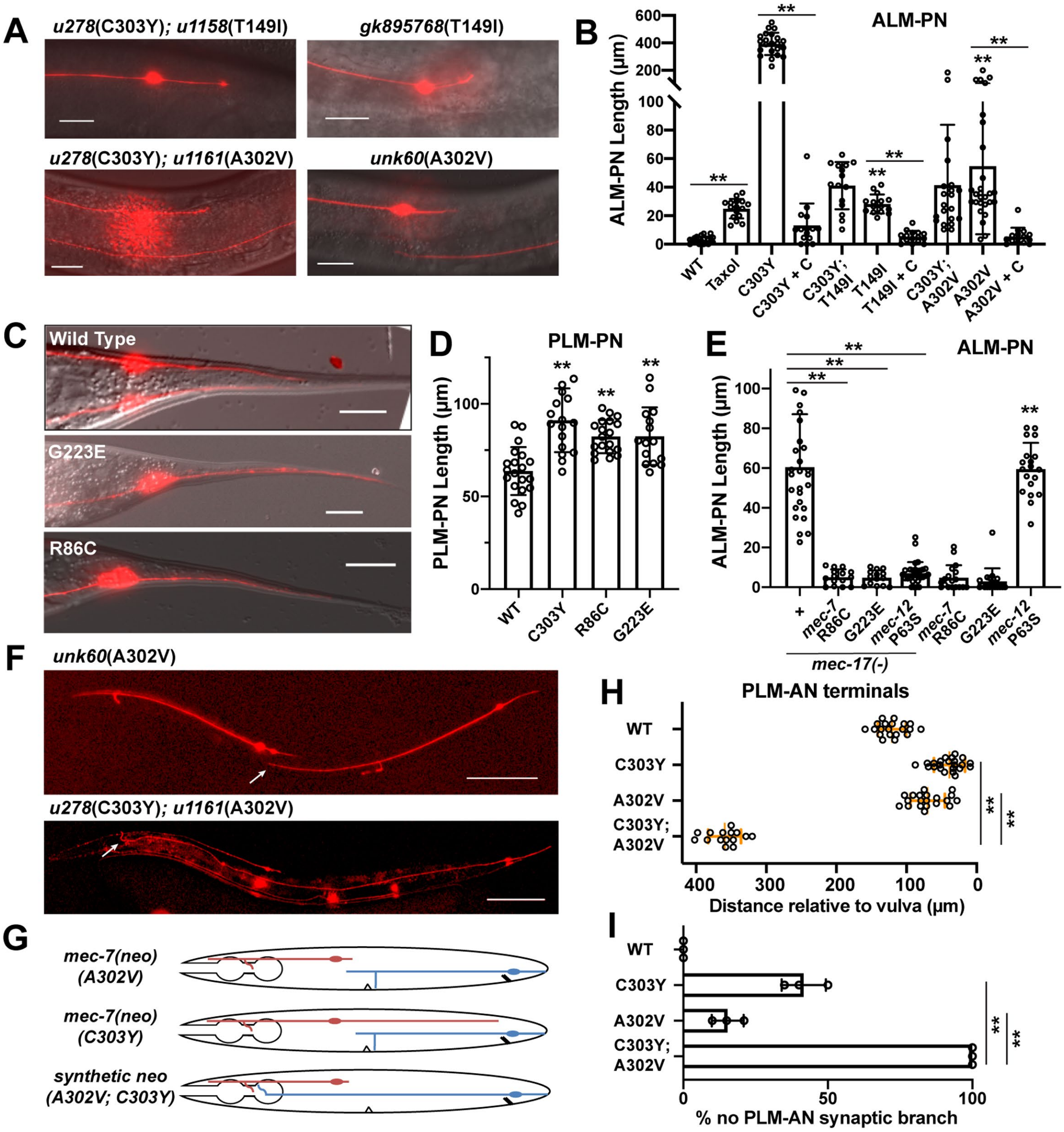

FIGURE 5: Epistatic and synthetic interaction between *mec-7* neomorphs. (A) Short ALM-PNs in animals carrying T149I and A302V single mutations of *mec-7* and the T149I C303Y and A302V C303Y double mutations. (B) Length of ALM-PNs in young adults of various mutants. Double asterisks indicate significant difference ($p < 0.01$). T149I and A302V single mutants were compared with WT. (C) Elongated PLM-PN in *mec-7* weak *neo* alleles carrying G223E or R86C mutation. (D) Quantification of PLM-PN length in young adults of indicated mutants. Double asterisks indicate significant difference ($p < 0.01$) compared with WT. (E) Length of ALM-PNs in young adults of *mec-17(-)*, *mec-7*(R86C), *mec-7*(G223E), and *mec-12*(P63S) single mutants and *mec-17(-)* double mutants with these *mec-7* and *mec-12* mutations. Double asterisks indicate significant difference ($p < 0.01$); *mec-12*(P63S) was compared with WT in B. (F) Anterior overextension of PLM-AN in *mec-7*(C303Y A302V) double mutants but not in *mec-7*(A302V) single mutants. (H) Distance from the PLM-AN terminals to the vulva in *mec-7 neo* single and double mutants. (G) Schematic diagram of ALM and PLM morphology in *mec-7 neo* single and double mutants. (I) The percentage of PLM-ANs that did not have synaptic branches in the indicated strains.

The substitution of A302, which is next to C303 on the H9-to-B8 loop, with either threonine (T) or valine (V) produced the characteristic ectopic ALM-PN of the *neo* phenotype. Since A302 is exposed on the MT surface (Figure 6A), its alteration may affect the interaction with certain MAPs. On the other hand, both A302T and A302V mutations led to clashes with D203 on H6, which helps form the GTP binding pocket (Figure 6E); thus, these substitutions may also affect GTP binding or the structural rearrangement related to GTP hydrolysis. T149 is located on H4 in the interior of β-tubulin (Figure 6A), and the neomorphic T149I mutation likely altered tubulin folding or heterodimer stability. Thus, the finding that T149I and A302V mutations could mask the effects of C303Y in promoting the growth of long ALM-PN might be explained by structural changes that led to the reshaping of the MAP binding surface or the alteration of overall heterodimer stability.

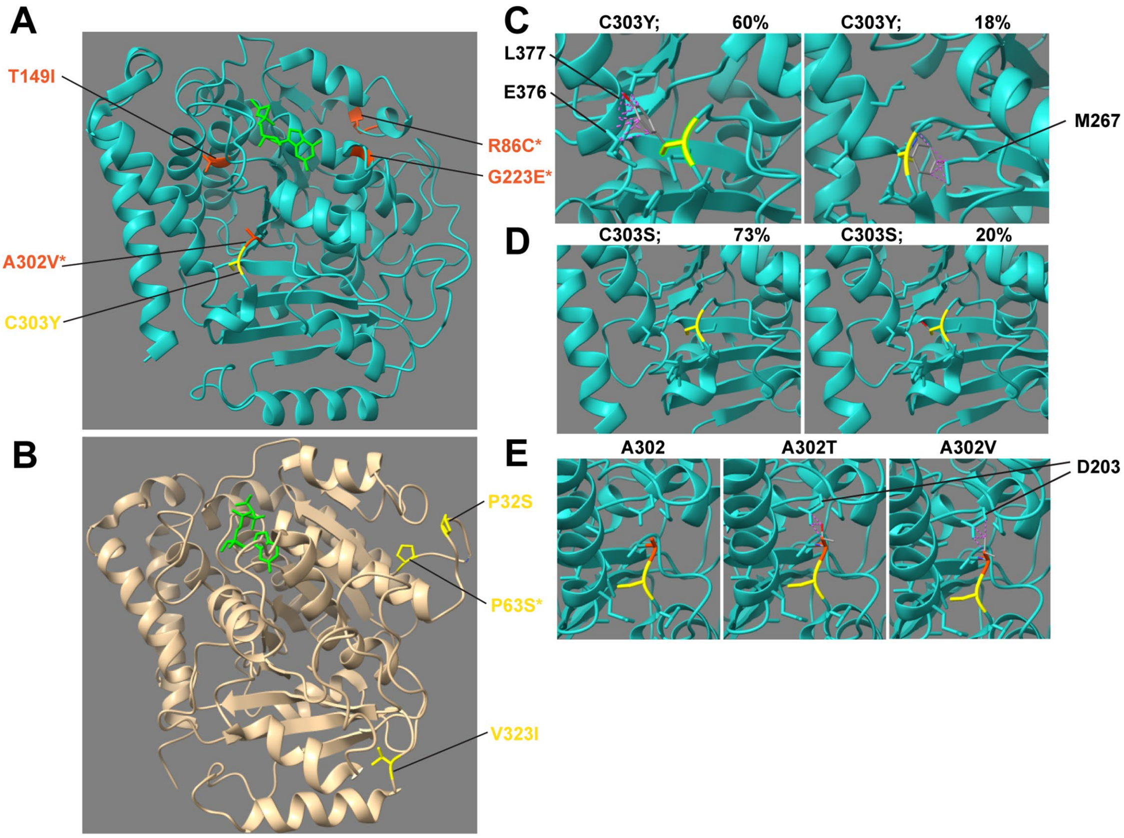

FIGURE 6: Structural modeling of the tubulin *neo* mutations. (A) Positions of the amino acids affected by *mec-7 neo* alleles. C303Y (yellow) is the strongest *mec-7 neo* alleles. Others (orange) are much weaker than C303Y mutation. (B) Positions of the amino acids affected by *mec-12 neo* alleles. In A and B, mutations with asterisks were isolated in this study and not analyzed before. (C) Modeling of the C303Y substitution with two possible orientations. Left panel shows a configuration with 60% possibility according to ChimeraX, which creates clashes (purple dashed lines) with L377 and E376 residues. Right panel shows another configuration with 18% possibility, leading to clashes with M267. (D) C303S substitution did not lead to any clashes with surrounding residues. (E) A302T and A302V substitutions led to clashes with D203 residue. C303 and A302 are labeled in yellow and orange, respectively.

Suppressors of *mec-17(-)* define a new type of *mec-7* neomorphs

Among the mutants isolated in the *mec-17(-)* suppressor screen, two *mec-7* alleles, *u1115*(R86C) and *u1114*(G223E), showed overextension of PLM-PN (a phenotype seen in *mec-7 neo* alleles) but not generation of an ectopic ALM-PN in single mutants (Figure 5, C–E). We classified this phenotype, which had not been seen before, as weak *neo*. R86 is located on the H2-to-B3 loop facing the lumen of MTs; G223 is located on H7 and is involved in lateral interaction. Neither of the two altered residues are mapped to the exterior surface of MTs and their substitutions did not have strong effects by themselves. Thus, the R86C and G223E mutations may increase MT stability slightly by affecting the tubulin folding or the lateral stacking of heterodimers. Their suppression of ALM-PN growth in *mec-17(-)* mutants was rather unexpected (Figure 5E).

In addition to being an α-tubulin acetyltransferase, MEC-17 has a genetically separable function in restricting neurite growth that is independent of its enzymatic activity (Topalidou *et al.*, 2012). Because MEC-17 acetylates MEC-12 at K40 localized on the H1-to-B2 loop (Akella *et al.*, 2010), one appealing hypothesis is that MEC-17 also plays a structural role by binding to the lumen-facing loops of MEC-12 to provide structural support for the MT organization and stability. In *mec-17(-)* mutants, the disorganization of the MTs may cause the growth of ectopic ALM-PN at the late L4 and early adult stages. The suppression of this excessive growth by the *lf* and *anti* alleles of *mec-7* and *mec-12* could be explained by their effects in inhibiting MT formation and neurite extension, whereas the suppression by the *mec-7 neo* alleles may be attributed to a moderate correction of the MT disorganization and instability. In fact, in addition to the ALM-PN phenotype, the swelling and bending of the TRN neurites in *mec-17(-)* mutants were also rescued by the R86C and G223E *neo* mutations in *mec-7* (Supplemental Figure S1B).

The *mec-17(-)* suppressor screen also yielded a *mec-12 neo* mutation *u1131*(P63S), which caused the growth of an ectopic ALM-PN in the *mec-17(+)* animals (Figure 5E). Surprisingly, the *mec-17(-) mec-12[u1131*(P63S)*]* double mutants had essentially no or very short ALM-PN, whereas the two singe mutants both had substantial ALM-PN growth. P63 is located in the interior lumen-facing H1-to-B2 loop, where K40 is also located (Figure 6B). Among the previously identified *mec-12 neo* mutations, P32S is also mapped to this H1-to-B2 loop. A third *neo* mutation V323I is mapped to the B8-to-H10 loop facing the lumen.

We suspect that these mutations may compensate for the destabilization induced by the loss of MEC-17 in the lumen, thus suppressing ALM-PN growth in *mec-17(-)* mutants. Two other previously identified *mec-12(neo)* mutations E196K and V260I were mapped to the exterior surface of MTs.

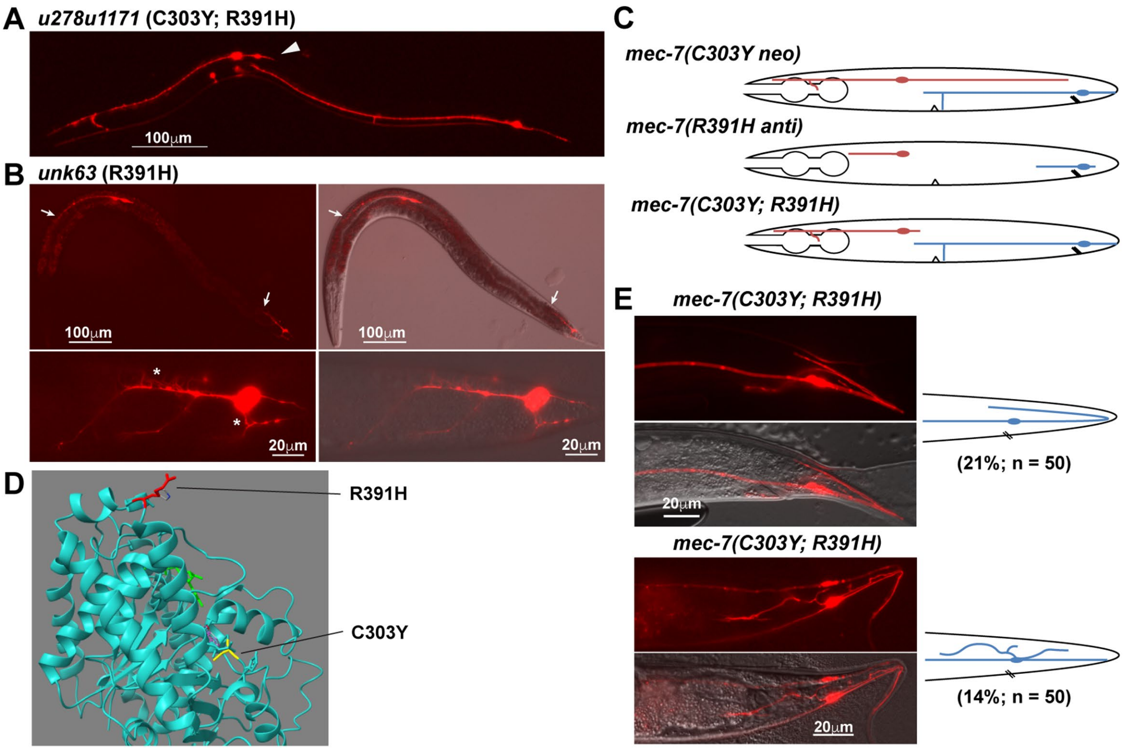

FIGURE 7: Balancing and synthetic interactions between *mec-7 neo* and *anti* alleles. (A) TRN morphology of animals carrying C303Y R391H double mutations in *mec-7*. Arrowhead points to the absence of long ALM-PN. (B) R391H single mutation caused an *anti* phenotype with severely shortened TRN neurites. Arrows point to the premature termination of ALM-AN and PLM-AN. The lower panels show the excessive short sprouts growing out of PLM-AN or PLM cell body in *mec-7*(R391H) mutants. (C) Schematic diagram of ALM and PLM morphologies in *mec-7 neo* and *anti* single mutants, as well as their double mutants. (D) The positions of R391 (red) and C303 (yellow) mutated in the two alleles. (E) Overextension of PLM-PN and excessive neurite sprouting from PLM cell body in the *mec-7*(C303Y R391H) double mutants. The diagrams on the right illustrate the abnormal PLM morphology at the tail.

Synthetic effects between *mec-7 neo* mutations

In addition to the suppression of *mec-7*(C303Y)-induced long ALM-PN by the intragenic A302V mutation, we surprisingly observed a remarkable overextension of PLM-AN in the animals carrying both A302V and C303Y mutation (Figure 5, F and G). This overextension was not observed in animals carrying either mutation alone. In fact, *u278*(C303Y) mutants had a slightly underextended PLM-AN; *unk60*(A302V) mutants, recreated in WT animals, had a PLM-AN with normal length (Figure 5H). To make sure this phenotype is not caused by a background mutation, we outcrossed the *u278u1161*(C303Y; C302V) mutants obtained from the screen five times and the overextended PLM-AN phenotype always segregated with the genotype of homozygous *u278u1161*. We also recreated C302V in the TU4879 [*mec-7(u278); uIs115(mec-17p::TagRFP)*] animals, the starter strain for the suppressor screen, through CRISPR gene editing, and obtained similar suppression of ALM-PN and overextension of PLM-AN. Thus, we conclude that the PLM-AN overextension is a synthetic phenotype of the A302V and C303Y mutations in *mec-7*.

We also observed an additive loss of PLM-AN synaptic branch. Around 15 and 40% of PLM-AN did not have a synaptic branch in *mec-7* animals carrying the A302V and C303Y mutation, respectively, whereas 100% of the double mutants did not grow the branch (Figure 5I). Similarly, some A302V and C303Y single mutants showed the mislocalization of synaptic vesicle protein GFP::RAB-3 into the neurite endings of ALM-PN and PLM-PN, whereas almost 100% of the double mutants had the posterior mistargeting phenotype (Supplemental Figure S2, C and D). The coexistence of epistatic, synthetic, and additive effects between *mec-7* neomorphs indicated that their genetic interaction is complex, which might result from the altered interaction with multiple MAPs in the double mutants.

Balancing and synthetic effects between *mec-7 neo* and *anti* mutations

Among the *mec-7* intragenic suppressors, *u278u1171*(C303Y; R391H) mutants had a strong or complete suppression of ALM-PN outgrowth but did not show any shortening of PLM-PN (Figure 7A). Thus, we were not able to estimate the effects of R391H single mutation based on the phenotype of the double mutant. We then recreated the R391H mutation in the otherwise WT background and found that this substitution alone led to a strong *anti* phenotype with all TRN neurites severely shortened (Figure 7B). Many sprouts and protrusions emanated from the PLM cell body and its short axon in *unk63*(R391H) mutants, likely a result of highly dynamic MTs (Figure 7B). This finding was rather unexpected, because we assumed that dominant-negative effects of *anti* mutations would be epistatic to the effects of the *neo* mutation. For example, both *u278u1154*(C303Y; E69K) and *u278u1170*(C303Y; P358S) double missense mutants showed the shortening of all TRN neurites similar to the typical *anti* alleles (Supplemental Figure S4, A and B; in addition to the P358S mutation found in this study, P357L and P358L mutations we previously isolated also caused *anti* phenotypes). Similarly, the *mec-7(u278); mec-12(anti)* double mutants showed the same phenotype (shortening of PLM-PN or PLM-AN) as the *mec-12(anti)* alleles alone (Supplemental Figure S4, C and D). Thus, the unexpected lack of neurite-shortening phenotype in *u278u1171*(C303Y; R391H) animals suggested that the MT-destabilizing effect of R391H substitution may be balanced by the stabilizing effect of C303Y mutation (Figure 7C).

R391 is located at the end of H11 (the 11th helix) and is exposed on the exterior surface of MTs (Figure 7D), which is unusual because most *anti* alleles affected residues involved in GTP binding and intradimer or interdimer interactions. We suspect that R391H substitution may disrupt the binding with certain MT-stabilizing MAPs or strengthen the interaction with some MT-destabilizing MAPs, which resulted in a strong reduction of MT stability. This reduction may be counterbalanced by C303Y substitution, which could have pushed H11 and R391 out of its normal position, so that the R391H substitution no longer has a disruptive effect on MT stability. Nevertheless, the suppression of ALM-PN growth by R391H mutation in *u278*(C303Y) animals suggested that neither of the two mutations is completely epistatic to the other. Their effects appeared to cancel each other out and a balance on the regulation of MT stability may have been achieved in the double mutants.

Although ~65% of the PLM neurons in the *u278u1171* double mutants had normal morphology, 21% of them had overextended PLM-PN that grew to the tip of the tail, turned, and then extended anteriorly for a short length, and 14% of the PLMs had one or two ectopic neurites emanating from the cell body (Figure 7E). These phenotypes were not observed in either *u278*(C303Y) or *unk63*(R391H) single mutants and appeared to be synthetic, indicating that the double substitution may lead to altered MT stability or dysregulation in neurite guidance in PLM neurons. Moreover, the fact that excessive neurite growth is suppressed in ALM neurons but exacerbated in PLM neurons in the *u278u1171* double mutants compared with *u278* single mutants suggests that MT regulation might differ in the two TRN subtypes.

DISCUSSION

A resource for phenotypic characterization of tubulin mutations

Understanding the cellular impact of tubulin mutations is of great interest not only to cell biologists but also to clinicians, given that over 100 tubulin missense mutations have been found to be associated with a range of cortical malformations, termed tubulinopathies (Romaniello *et al.*, 2018). We previously proposed to use the *C. elegans* TRNs as a model to study the effects of tubulin mutation on MT stability and neuronal morphogenesis and reported the phenotype of 67 tubulin missense mutations on neurite growth (Zheng *et al.*, 2017). This study, through suppressor screens, isolated and characterized 32 new mutations, thus bringing the total number of tubulin missense mutations in our collection to 99 (Table 1). To our knowledge, this is so far the largest collection of tubulin mutations with phenotypic characterization in neurons. These data may serve as a resource to help evaluate the effect of specific amino acid substitutions on MT functions during neuronal development.

Studies of the tubulin mutations also suggested that correct neurite growth pattern requires optimal MT stability. Reduction in MT stability (or increased dynamics) resulted in neurite growth defects in ALM and PLM neurons, and the level of the reduction correlated with the severity of the defects. For example, slight down-regulation of MT stability in *mec-7* partial *lf* mutants caused the loss of the PLM synaptic branch first, further reduction in *mec-7 lf* mutants led to the shortening of PLM-PN, and strong destabilization of MTs in the *anti* mutants severally truncated all neurites, including ALM-AN, PLM-AN, and PLM-PN. The reason that PLM-PN is more sensitive to MT destabilization than ALM-AN and PLM-AN may be that PLM-PN has fewer MTs (~17 MTs per cross section) than the other two neurites (~30 MTs per cross section) (Chalfie and Thomson, 1979) and that PLM-PN has mixed MT polarity, whereas the other two neurites have uniform plus-end-out MT polarity (Figure 3). Furthermore, mixed MT polarity may be correlated with shorter neurites in the TRNs. *mec-7 lf* and *anti* mutations led to mixed polarity in PLM-AN and neurite growth defects.

On the other hand, elevated MT stability and reduced dynamics in *mec-7* and *mec-12 neo* mutants led to the formation of the ectopic ALM-PN in ALM neurons. *mec-7(neo)* mutants also caused the elongation of PLM-PN, which was correlated with the conversion from mixed MT polarity to uniform plus-end-out polarity. This observation supports the connection between MT polarity and neurite extension. Nevertheless, PLM neurons did not seem to grow an extra neurite in the *neo* mutants. Normally ALM neurons are unipolar and PLM neurons are bipolar. Although ALM was able to extend a long neurite toward the posterior when MT became abnormally stable, the inability of PLM neurons to grow a third neurite suggested that neurite growth is under the control of various guidance cues (e.g., Wnt signals) and simple alteration of MT stability would not change the general neurite growth pattern along the longitudinal tracks of these neurons.

Connecting tubulin mutation phenotypes across species and to clinical symptoms

Recently, an online database called "The tubulin mutation database" was built to compile the phenotypes of missense tubulin mutations in different experimental systems, as well as clinical studies (Hussey and Fritz-Laylin, 2019; Pham and Morrissette, 2019). This database allowed us to compare phenotypes across species and to connect cellular defects to clinical symptoms. For example, among the newly identified *mec-7*/β-tubulin mutations, E3K and D203V caused the *lf* phenotype with a shortened PLM-PN and R121K led to a partial *lf* phenotype with the loss of the PLM synaptic branch. All three mutations likely decreased MT stability. Substitution of the same amino acids (E3A, D203A, and R121A) in yeast led to benomyl supersensitivity, which is indicative of less stable MTs (Reijo *et al.*, 1994). Similarly, G146E mutation in *mec-7* led to a *lf* phenotype in our studies and G146C mutation in mouse β1 tubulin rendered the protein incapable of forming heterodimers with α-tubulin (Zabala *et al.*, 1996). Consistency across different organisms highlights the evolutionary conservation of tubulin functions and suggests that results from one organism can provide insight for studies in another.

Mutations newly identified in this study also have clinical relevance, since the same mutations or mutations affecting the same amino acids were also found in patients with neurological diseases. For example, the dominant, antimorphic R320C mutation in *mec-12*/α-tubulin was found among the human TUBA4A mutations associated with familial amyotrophic lateral sclerosis (Smith *et al.*, 2014). Interestingly, when incorporated into the MTs, TUBA4A R320C mutants disrupted MT polymerization and stability through a dominant-negative mechanism in transfected COS7 cells (Smith *et al.*, 2014). Thus, the effect of the human disease-associated mutation is highly consistent with its effect in *C. elegans* TRNs. Similarly, in human TUBB2B, G13A mutation was associated with cerebellar dysplasia (Oegema *et al.*, 2015) and G98R was associated with cortical malformation, such as polymicrogyria and microlissencephaly (Cushion *et al.*, 2013). These clinical symptoms are related to defects in neuronal differentiation and axonal growth, consistent with our findings that mutations affecting the same amino acids in *mec-7* (G13S and G98E) led to *lf* phenotype. Moreover, R391H mutation in human TUBB4B caused Leber congenital amaurosis, a neurodegenerative disease of photoreceptor cells; this mutant TUBB4B can form α/β-heterodimers and incorporate into the MT lattice but would disrupt the MT dynamics and significantly dampen normal MT growth (Luscan *et al.*, 2017). Very similarly, the same R391H mutation in *mec-7* was antimorphic and severely impaired neurite growth.

The above examples support the utility of *C. elegans* TRNs as a testing platform to assess the cellular impact of disease-associated tubulin mutations and to connect the defects at the single cell level to clinical manifestation. Given the ease of gene editing in *C. elegans*, we envision that human tubulin mutations can be routinely installed in *mec-7* and *mec-12* and their effect on MT functions and neuronal growth can be quickly evaluated.

Genetic interactions among tubulin mutants

Ever since the pioneering work on the tubulins in *Aspergillus nidulans* (a filamentous fungus) by Ron Morris (Sheir-Neiss *et al.*, 1978; Morris *et al.*, 1979), molecular genetics approaches have been used to study the function of tubulins and MTs in various biological processes. For example, a missense mutation in the β-tubulin gene *ben*A in *A. nidulans* called *ben*A33 (Q134K) caused a temperature-sensitive hyperstabilization of kinetochore MTs, which inhibited the movement of chromosomes to the mitotic poles and blocked growth at 42°C (Oakley and Morris, 1981; Jung *et al.*, 1998). This *ben*A33 allele was used as a sensitized background to identify revertants that restored growth at the restrictive temperature, which led to the discovery of an α-tubulin gene *tub*A (all 14 extragenic suppressors were mapped to tubA; Morris *et al.*, 1979). These results also suggested the interdependence of α- and β-tubulin genes. Similarly, our work focusing on neuronal MTs used a *neo* mutation of *mec-7*/β-tubulin that elevated MT stability in a revertant screen and identified both intragenic suppressors in *mec-7* and extragenic suppressors in *mec-12*/α-tubulin. Our finding that *lf* and *anti* mutations in *mec-7* and *mec-12* are mostly epistatic to the *neo* mutation is consistent with earlier studies and support that the functions of α- and β-tubulin genes are dependent on each other.

In this study, we also observed additive or synergistic effects among the *mec-7*/β-tubulin neomorphs that presumably increased MT stability. The combination of A302V and C303Y mutations increased the penetrance for the loss of PLM synaptic branches and the mistargeting of synaptic vesicle proteins, compared with either single mutation. In a more extreme case, animals carrying the double mutations also showed a synthetic phenotype of PLM-AN overextension, which was not seen at all in the two single mutants. We suspect that the A302V; C303Y double mutations may affect the association of certain MAPs and render MTs resistant to MT-destabilizing signals at the growth cone during axonal termination, e.g., RPM-1 signaling (Borgen *et al.*, 2017). Overall, our observations suggest that the independent effects of single tubulin mutations can be combined to create enhanced or sometimes synthetic effects.

Additive effects of tubulin mutations have also been seen in other organisms. For example, the combination of two pesticide-resistant α-tubulin mutations T239I and M268T found in the goosegrass *Eleusine indica* showed increased pesticide resistance compared with either mutation on its own (Anthony and Hussey, 1999). Similarly, compared with the single mutation E198A in β-tubulin, three double mutations E198A; M163I, E198A; F167Y, and E198A; F200S conferred significantly increased resistance to benzimidazoles in another filamentous fungi *Corynespora cassiicola* (Duan *et al.*, 2019). In Drosophila, recessive *lf* mutations in the testis-specific β2-tubulin gene (*B2t*) failed to complement with the likely antimorphic V177M mutation in an α-tubulin gene for the male sterility phenotype (Hays *et al.*, 1989), suggesting that additive effects also occur between mutations of α- and β-tubulin genes.

In addition to the above genetic interactions, our work also identified some unexpected interactions among the tubulin mutations. One such interaction is the epistasis among the *mec-7 neo* mutations. We found that weaker *neo* changes, such as T149I and A302V mutations, could suppress the stronger *neo* mutation *u278*(C303Y). This result indicates that tubulin mutations producing similar phenotypes can not only be additive with each other but also be epistatic to each other. The molecular basis for this epistasis may result from the structural change caused by one mutation becoming functionally ineffective in the presence of another mutation, perhaps by the subsequent change of tubulin structures or interactions with MAPs. This intramolecular epistasis may fit into the category of "conformational epistasis" defined by Ben Lehner (2011).

Another unexpected interaction is the balancing effect between the *mec-7 neo* change C303Y and the *anti* change R391H. In most cases, we expected and observed *anti* mutations being epistatic to *neo* mutations, since *anti* mutations often cause structural alterations that render the tubulin protein toxic and block MT polymerization. R391H mutation may be an exception because R391 is exposed on the surface of MTs and its substitution might affect the interaction with certain MAPs. If the C303Y(*neo*) and R391H(*anti*) mutations impact the association of MAPs with opposite functions (e.g., MT-stabilizing vs. -destabilizing), one may expect their effects to neutralize each other.

The above examples reveal a previously underappreciated complexity in the genetic interactions among tubulin mutations. Since each mutation may alter tubulin structure or function in unique ways, structural modeling and functional characterization are needed to determine the combinatorial effects of different tubulin mutations.

MATERIALS AND METHODS

Request a protocol through Bio-protocol.

Strains and transgenes

C. elegans WT (N2) and mutant strains were maintained at 20°C as previously described (Brenner, 1974). Alleles used in this study are described in the main text. Most strains were provided by the Caenorhabditis Genetics Center, which is funded by the National Institutes of Health (NIH) Office of Research Infrastructure Programs (P40 OD010440). Transgenes *uIs115[mec-17p::TagRFP] IV*, *uIs134[mec-17p::TagRFP] V*, *uIs31[mec-17p::GFP] III*, and *uIs110[mec-17p::TagRFP; sto-5p::GFP]* were used to visualize TRNs. Transgene *jsIs821[mec-7p::GFP::rab-3] X* was used to visualize the transport of synaptic proteins.

Suppressor screens

For the *mec-7(neo)* suppressor screen, we used TU4879 [*mec-7(u278) X; uIs115(mec-17p::TagRFP) IV*] as the starter strain, which showed the growth of a long ALM-PN, and ethyl methanesulfonate (EMS) as the mutagen (Brenner, 1974). After screening through 53,600 haploid genomes, we isolated 30 mutants that showed very short or no ALM-PN and outcrossed the mutants against TU4879 and identified the phenotype-causing mutations through a combination of whole-genome resequencing, candidate gene sequencing, and complementation tests (Supplemental Table S1).

For *mec-17(-)* suppressor screen, we used TU6216 [*mec-17(ok2109) IV; uIs110(mec-17p::TagRFP; sto-5p::GFP) II*] as the starter strain, which grew a ALM-PN with moderate length in L4 animals and young adults. By screening through 15,000 haploid genomes, we isolated in total 31 mutants that had very short or no ALM-PN in day 1 adults and identified 16 *mec-7* and 10 *mec-12* mutations by targeted sequencing (Supplemental Table S2).

CRISPR/Cas9-mediated gene editing

To create *mec-7* alleles, *unk64*(R121K), *unk62*(A254T), *unk60*(A302V), and *unk63*(R391H) in the WT background, we performed CRISPR/Cas9-mediated gene editing in TU4065 [*uIs115(Pmec-17::RFP) IV*] animals using a previously reported method (Dokshin *et al.*, 2018). Briefly, sgRNAs targeting specific sequences in *mec-7* were synthesized using the EnGen sgRNA Synthesis Kit (E3322V) from New England Biolabs (NEB; Ipswich, MA) and purified using NEB Monarch RNA Cleanup Kit (T2030L); 1 µg of the sgRNA was injected into *C. elegans* together with 20 pmol recombinant Cas9 (EnGen *S. pyogenes* Cas9 NLS from NEB, M0646T) and 1µg ssDNA repair donor for homologous recombination. Synonymous mutations were included in the repair template to avoid the digestion by Cas9. pCFJ104 (*myo-3p::mCherry*) was used as a co-injection marker and the transformants with red muscles were genotyped for successful incorporation of the repair template. CRISPR target sequences and repair donor sequences used to generate the above alleles are shown in Supplemental Table S3.

Structural modeling

Missense mutations in *mec-7* and *mec-12* were mapped to the structure of *Bos taurus* α/β tubulin (1JFF in PDB). Molecular graphics and analyses were performed with University of California, San Francisco (UCSF) ChimeraX (macOS 10.13; https://www.rbvi.ucsf.edu/chimerax/, developed by the Resource for Biocomputing, Visualization, and Informatics at UCSF with support from NIH R01-GM129325 and the Office of Cyber Infrastructure and Computational Biology, National Institute of Allergy and Infectious Diseases; Goddard *et al.*, 2018). The effects of amino acid substitution were modeled using the "Structure Editing/Rotamer" function of ChimeraX and the Dunbrack rotamer library (Shapovalov and Dunbrack, 2011). Only the positions with high probability of substituted amino acids were shown. To model the clashes, pairs of atoms with VDW overlap ≥0.6 Å were identified; 0.4 Å were subtracted from the overlap for potentially H-bonding pairs. The numbering of α-helices (H1 to H12) and β-strands (B1 to B10) was based on the α/β tubulin dimer structure (Nogales *et al.*, 1998).

Pharmacological treatment and EBP-2 tracking

To treat various animals with MT-destabilizing and -stabilizing agents, colchicine and paclitaxel (taxol) were added to the NGM plates for a final concentration of 1 and 1 µM, respectively. L1 animals were placed onto the plates and grew to day 1 adults to be analyzed.

To study MT dynamics, we crossed *juIs338[mec-4p::ebp-2::GFP + ttx-3p::RFP]*, which expressed EBP-2::GFP in TRNs specifically, with various tubulin mutants. We then mounted day 1 adults on agarose pad and immobilized the animals with 100-nm polystyrene beads and imaged the TRNs for 1 min. The number of EBP-2::GFP tracks within 60 µm from the cell body were counted for PLM-AN and within 25 µm for PLM-PN. About 10 animals were imagined for each strain. For the colchicine treatment, L4 animals were placed onto a plate with 0.125 mM colchicine for 8 h and then recovered on a regular NGM plate for 1 h before imaging.

Phenotype scoring and statistical analysis

Fluorescent imaging was done on a Leica DMi8 inverted microscope equipped with a Leica DFC7000 GT monochrome camera. Measurements were made using the Leica Application Suite X (3.7.0.20979) software.

We measured the length of ALM-PN and PLM-PN in at least 20 day 1 adults grown at 20°C. Defects in PLM-AN growth were assessed by measuring the distance from the PLM-AN terminals to the center of the vulva. Positive numbers mean PLM-AN terminals are more anterior than the vulva; negative numbers mean PLM-AN did not reach the vulva; at least 20 cells were examined for each strain. All bar graphs show mean ± SD.

Fluorescence intensity of the TagRFP expressed from the *uIs115[mec-17p::TagRFP]* transgene in the PLM cell body was used to measure TRN protein levels; intensity was measured by first acquiring images using the identical exposure time and laser power and then manually subtracting the background from the fluorescent signal using Leica Application Suite X (3.7.0.20979). At least 20 cells were imaged and analyzed for each strain.

For statistical analysis, analysis of variance and the post hoc Dunnett's test (comparison of each of many treatments with a single control) were performed using the GraphPad Prism (version 8.4.0 for Mac, GraphPad Software, La Jolla, CA; www.graphpad.com) to identify significant difference among samples. Single and double asterisks indicate $p < 0.05$ and $p < 0.01$, respectively. All measurements were repeated three times on different days and similar results were obtained; data from one representative trial were shown.

ACKNOWLEDGMENTS

We thank Alice Niu and Mona Liu at Columbia University for helping with the *mec-17(-)* suppressor screen. We acknowledge support from the Research Grant Council of Hong Kong (ECS 27104219 to C.Z.), the Food and Health Bureau of Hong Kong (HMRF 07183186 to C.Z.), seed funds from the University of Hong Kong (201812159005 and 201910159087 to C.Z.), and the NIH (GM30997 and GM122522 to M.C.).

REFERENCES

Akella JS, Wloga D, Kim J, Starostina NG, Lyons-Abbott S, Morrissette NS, Dougan ST, Kipreos ET, Gaertig J (2010). MEC-17 is an alpha-tubulin acetyltransferase. Nature 467, 218–222.

Anthony RG, Hussey PJ (1999). Double mutation in eleusine indica alpha-tubulin increases the resistance of transgenic maize calli to dinitroaniline and phosphorothioamidate herbicides. Plant J 18, 669–674.

Bahi-Buisson N, Poirier K, Fourniol F, Saillour Y, Valence S, Lebrun N, Hully M, Bianco CF, Boddaert N, Elie C, *et al.* (2014). The wide spectrum of tubulinopathies: what are the key features for the diagnosis? Brain 137, 1676–1700.

Basciano PA, Matakas J, Pecci A, Civaschi E, Cagioni C, Bompiani N, Burger P, Christos P, Snyder JP, Bussel J, *et al.* (2015). beta-1 tubulin R307H SNP alters microtubule dynamics and affects severity of a hereditary thrombocytopenia. J Thromb Haemost 13, 651–659.

Borgen MA, Wang D, Grill B (2017). RPM-1 regulates axon termination by affecting growth cone collapse and microtubule stability. Development 144, 4658–4672.

Bounoutas A, Kratz J, Emtage L, Ma C, Nguyen KC, Chalfie M (2011). Microtubule depolymerization in Caenorhabditis elegans touch receptor neurons reduces gene expression through a p38 MAPK pathway. Proc Natl Acad Sci USA 108, 3982–3987.

Brenner S (1974). The genetics of Caenorhabditis elegans. Genetics 77, 71–94.

Chalfie M, Thomson JN (1979). Organization of neuronal microtubules in the nematode Caenorhabditis elegans. J Cell Biol 82, 278–289.

Cushion TD, Dobyns WB, Mullins JG, Stoodley N, Chung SK, Fry AE, Hehr U, Gunny R, Aylsworth AS, Prabhakar P, *et al.* (2013). Overlapping cortical malformations and mutations in TUBB2B and TUBA1A. Brain 136, 536–548.

Dokshin GA, Ghanta KS, Piscopo KM, Mello CC (2018). Robust genome editing with short single-stranded and long, partially single-stranded DNA donors in Caenorhabditis elegans. Genetics 210, 781–787.

Duan Y, Xin W, Lu F, Li T, Li M, Wu J, Wang J, Zhou M (2019). Benzimidazole- and QoI-resistance in Corynespora cassiicola populations from greenhouse-cultivated cucumber: An emerging problem in China. Pestic Biochem Physiol 153, 95–105.

Goddard TD, Huang CC, Meng EC, Pettersen EF, Couch GS, Morris JH, Ferrin TE (2018). UCSF ChimeraX: Meeting modern challenges in visualization and analysis. Protein Sci 27, 14–25.

Hays TS, Deuring R, Robertson B, Prout M, Fuller MT (1989). Interacting proteins identified by genetic interactions: a missense mutation in alpha-tubulin fails to complement alleles of the testis-specific beta-tubulin gene of Drosophila melanogaster. Mol Cell Biol 9, 875–884.

Hsu JM, Chen CH, Chen YC, McDonald KL, Gurling M, Lee A, Garriga G, Pan CL (2014). Genetic analysis of a novel tubulin mutation that redirects synaptic vesicle targeting and causes neurite degeneration in C. elegans. PLoS Genet 10, e1004715.

Hussey SP, Fritz-Laylin LK (2019). "The missing link": the tubulin mutation database connects over 1500 missense mutations with phenotypes across eukaryotes. Cytoskeleton (Hoboken) 76, 175–176.

Jung MK, May GS, Oakley BR (1998). Mitosis in wild-type and beta-tubulin mutant strains of Aspergillus nidulans. Fungal Genet Biol 24, 146–160.

Lehner B (2011). Molecular mechanisms of epistasis within and between genes. Trends Genet 27, 323–331.

Luscan R, Mechaussier S, Paul A, Tian G, Gerard X, Defoort-Dellhemmes S, Loundon N, Audo I, Bonnin S, LeGargasson JF, *et al*. (2017). Mutations in TUBB4B cause a distinctive sensorineural disease. Am J Hum Genet 101, 1006–1012.

Morris NR, Lai MH, Oakley CE (1979). Identification of a gene for alpha-tubulin in Aspergillus nidulans. Cell 16, 437–442.

Nogales E, Wolf SG, Downing KH (1998). Structure of the alpha beta tubulin dimer by electron crystallography. Nature 391, 199–203.

Oakley BR, Morris NR (1981). A beta-tubulin mutation in Aspergillus nidulans that blocks microtubule function without blocking assembly. Cell 24, 837–845.

Oegema R, Cushion TD, Phelps IG, Chung SK, Dempsey JC, Collins S, Mullins JG, Dudding T, Gill H, Green AJ, *et al*. (2015). Recognizable cerebellar dysplasia associated with mutations in multiple tubulin genes. Hum Mol Genet 24, 5313–5325.

Pham CL, Morrissette NS (2019). The tubulin mutation database: A resource for the cytoskeleton community. Cytoskeleton (Hoboken) 76, 186–191.

Reijo RA, Cooper EM, Beagle GJ, Huffaker TC (1994). Systematic mutational analysis of the yeast beta-tubulin gene. Mol Biol Cell 5, 29–43.

Romaniello R, Arrigoni F, Fry AE, Bassi MT, Rees MI, Borgatti R, Pilz DT, Cushion TD (2018). Tubulin genes and malformations of cortical development. Eur J Med Genet 61, 744–754.

Shapovalov MV, Dunbrack RL Jr (2011). A smoothed backbone-dependent rotamer library for proteins derived from adaptive kernel density estimates and regressions. Structure 19, 844–858.

Sheir-Neiss G, Lai MH, Morris NR (1978). Identification of a gene for beta-tubulin in Aspergillus nidulans. Cell 15, 639–647.

Smith BN, Ticozzi N, Fallini C, Gkazi AS, Topp S, Kenna KP, Scotter EL, Kost J, Keagle P, Miller JW, *et al*. (2014). Exome-wide rare variant analysis identifies TUBA4A mutations associated with familial ALS. Neuron 84, 324–331.

Ti SC, Pamula MC, Howes SC, Duellberg C, Cade NI, Kleiner RE, Forth S, Surrey T, Nogales E, Kapoor TM (2016). Mutations in human tubulin proximal to the kinesin-binding site alter dynamic instability at microtubule plus- and minus-ends. Dev Cell 37, 72–84.

Tischfield MA, Cederquist GY, Gupta ML Jr, Engle EC. (2011). Phenotypic spectrum of the tubulin-related disorders and functional implications of disease-causing mutations. Curr Opin Genet Dev 21, 286–294.

Topalidou I, Keller C, Kalebic N, Nguyen KC, Somhegyi H, Politi KA, Heppenstall P, Hall DH, Chalfie M (2012). Genetically separable functions of the MEC-17 tubulin acetyltransferase affect microtubule organization. Curr Biol 22, 1057–1065.

Zabala JC, Fontalba A, Avila J (1996). Tubulin folding is altered by mutations in a putative GTP binding motif. J Cell Sci 109 (Pt 6), 1471–1478.

Zheng C, Atlas E, Lee HMT, Jao SLJ, Nguyen KCQ, Hall DH, Chalfie M. (2020). Opposing effects of an F-box protein and the HSP90 chaperone network on microtubule stability and neurite growth in Caenorhabditis elegans. Development 147.

Zheng C, Diaz-Cuadros M, Nguyen KCQ, Hall DH, Chalfie M (2017). Distinct effects of tubulin isotype mutations on neurite growth in Caenorhabditis elegans. Mol Biol Cell 28, 2786–2801.